Evaluation of 3D Reconstruction Algorithms for a Small Animal PET Camera

C.A. Johnson[1], *Member, IEEE,* J. Seidel[2], R.E. Carson[3], *Member, IEEE,*
W.R. Gandler[1], *Senior Member, IEEE,* A. Sofer[4*] , M.V. Green[2], and
M.E. Daube-Witherspoon[3], *Member, IEEE*

[1]Division of Computer Research and Technology
[2]Nuclear Medicine Department, Clinical Center
[3]PET Department, Clinical Center
National Institutes of Health, Bethesda, MD 20892
[4]George Mason University, Fairfax, VA 22030

Abstract

The use of paired, opposing position-sensitive phototube scintillation cameras (SCs) operating in coincidence for small animal imaging with positron emitters is currently under study. Because of the low sensitivity of the system even in 3D mode and the need to produce images with high resolution, it was postulated that a 3D expectation maximization (EM) reconstruction algorithm might be well suited for this application. We investigated six reconstruction algorithms for the 3D SC PET camera: 2D filtered back-projection (FBP), 3D reprojection (3DRP), 2D EM, 3D EM, 2D ordered subset EM (OSEM), and 3D OSEM. Noise was assessed for all slices by the coefficient of variation in a simulated uniform cylinder. Resolution was assessed from a simulation of 15 point sources in the warm background of the uniform cylinder. At comparable noise levels, the resolution achieved with EM and OSEM (0.9-mm to 1.2-mm) is significantly better than that obtained with FBP or 3DRP (1.5-mm to 2.0-mm.) Images of a rat skull labeled with ^{18}F-fluoride suggest that 3D EM and 3D OSEM can improve image quality of a small animal PET camera.

I. INTRODUCTION

Dedicated small animal PET systems are designed with a goal of optimizing spatial resolution while maintaining detection sensitivity [1,2]. Because spatial resolutions on the order of 1 mm may be required in small animal PET studies, the resolution of the reconstructed image generally limits the quality and quantitative accuracy of these studies [3]. Resolution can be improved using recovery methods at the cost of potentially increased noise [4,5]. The counting statistics of the study must therefore be reasonably high if resolution recovery is to be attempted. Higher tracer doses, however, may cause biochemical saturation in the system under study, e.g. receptor systems [6]. Thus it may be unreasonable to assume that good statistics can be achieved by increasing the dose. By including axially oblique lines of response (LORs), 3D acquisition (and reconstruction) can dramatically improve the sensitivity of the system.

In this paper, we consider a small animal PET scanner consisting of opposed NaI(Tl) crystals optically coupled to position-sensitive photomultipier tubes (PSPMT) [7]. The low stopping power of the thin (4-mm) NaI(Tl) scintillator crystals limits the sensitivity of the system. The camera under study can accept axial coincidence angles of up to 21.9^{o}. Fourier-based reconstruction methods require complete data sets, but systems with large axial acceptance angles generate increasingly incomplete data sets. The 3D Reprojection reconstruction algorithm (3DRP) estimates the missing data by forward-projecting a 2D filtered backprojection (FBP) reconstruction [8,9].

Liow, Strother, and Rottenberg have reported that 3D expectation maximization (EM) reconstructions possess improved resolution over 3DRP reconstructions in a clinical PET system [10]. Through a maximum likelihood criterion, the EM reconstruction algorithm models the Poisson nature of the observations. We hypothesize that maximum likelihood reconstructions may offer an advantage in a low count, finely sampled situation such as that under study here. EM can also incorporate the resolution limitations of the detection system into the reconstruction model and thereby remove the partial volume effect inherent in FBP [4]. Liow and Strother have reported moderately improved noise in EM reconstructions at matched resolutions relative to FBP [11].

In this investigation we compare 2D FBP and 3DRP reconstructions with 2D EM and 3D EM reconstructions for an opposed-mode NaI(Tl) PET scanner with very fine sampling. Hudson and Larkin have reported that ordered subset EM (OSEM) with k subsets taken to n/k iterations can produce reconstructions with similar image quality as EM taken to n iterations [12]. Since the computational costs of performing 3D EM reconstructions on large data sets can be high, we also compare the 2D FPB and 3DFP reconstructions with 2D OSEM and 3D OSEM reconstructions, respectively.

II. METHODS

A. Scanner Geometry

Figure 1 provides a schematic illustration of the small

animal scanner used in this study. The imaging system consists of two opposing NaI(T1) PSPMT cameras [8], each 6-cm horizontally × 5-cm vertically and separated by 12.8-cm center-to-center. The PSPMTs provide a continuous readout which is sampled onto 0.234-mm square detection bins. The object is rotated at least one full revolution in order to obtain a complete data set. At the center of the field of view, each camera has a point spread function with full width at half maximum (FWHM) 1.0-mm, and the coincidence point spread function has a FWHM of 1.2-mm.

Data were converted from list-mode into 3D sinograms (90 million LORs) and 2D sinograms (850,000 LORs). Coincidences corresponding to axial angles greater than 13.6° were not included to reduce computation time. The 3D reconstructed object consists of 128×128×107 cubic voxels (.47-mm)^3. In 2D, the reconstructed object has 23 2.1-mm thick slices of 128×128 pixels (.47-mm)^2. Corrections for redundant sampling of LORs and radioactive decay were included in the reconstructions; no other corrections were incorporated.

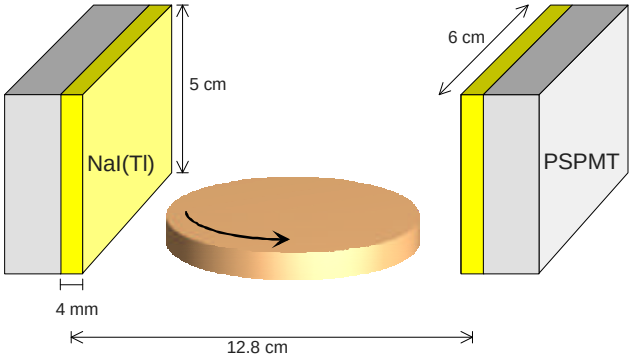

Figure 1: Schematic illustration of opposed-mode NaI(Tl) scanner.

B. Reconstruction Algorithms

The ordered subset EM (OSEM) algorithm partitions the projections into k subsets. Each OSEM iteration performs forward- and back-projections sequentially on the k subsets. Hudson and Larkin have reported that this technique results in convergence acceleration of approximately k over EM for small k [12].

The EM and OSEM reconstructions were performed on an IBM SP2 parallel computer. The parallel implementation decomposes projection space according to base-symmetry angles and incorporates symmetries in the EM system matrix to reduce the storage requirement [13]. Each processor thus performs forward- and back-projections on its portion of base-symmetry angles and their symmetry related angles. In OSEM, the projection space is also decomposed into OSEM subsets. The OSEM partitioning is in fact the primary decomposition; the parallel partitioning is performed within each subset.

We have discovered that in order to obtain a valid result in 3D OSEM, each reconstructed axial slice must be represented in each OSEM sub-iteration. If OSEM subsets are assigned by partitioning the in-plane (azimuthal) angles evenly amongst the subsets, this requirement is satisfied. Every subset then covers the same group of in-plane angles over all axial angles and axial offsets. Each in-plane angle is related by symmetry to 8 other in-plane angles. Let L be the number of in-plane angles and $h=L/8$ be the integer number of base-symmetry in-plane angles. The OSEM partitioning strategy used here assigns the h base-symmetry in-plane angles in a modulus fashion to the k subsets. If h is an integer muliple of k, the base-symmetry angles partition evenly as required. In this study we have used L=480 and k=5.

For each of the studies described below, we performed 6 reconstructions: 2D FBP, 3DRP, 2D EM, 3D EM, 2D OSEM, and 3D OSEM. Although EM and OSEM can incorporate a spatially-varying resolution model, for these studies a uniform 1.2-mm Gaussian model was used. In EM and OSEM, forward- and back-projections were only performed for those LORs with at least one count in order to improve computational performance.

C. Noise/Resolution Study

A numerical phantom consisting of 15 ideal point sources in a warm cylinder was used to quantify the noise and resolution properties of the algorithms. The data were generated by a Monte Carlo simulation of the scanner that realistically models the ^{18}F positron range and non-colinearity as well as depth of interaction effects and crystal scatter. The simulation ignores randoms, the effects of attenuation and object scatter, and spatial nonuniformities in the scanner's resolution.

The ideal point sources were placed in 3 axial planes, z={-20, 0, 10}-mm. In each plane the point sources were located at radial positions r={0, 4, 8, 12, 16}-mm. In the simulation, 100K counts were used for all 15 points, while 5M counts were used for the cylinder. A Gaussian curve fit (including background) of the reconstructed point sources was used to measure resolution, parameterized by the FWHM in all 3 directions. The cylinder was 4 cm in diameter, centered in the transverse plane and covering the entire axial field of view (5-cm). Noise was measured in each reconstructed slice by calculating the coefficient of variation (COV) over 12 regions of interest (ROIs), each comprising 256 pixels. The COV of each ROI is defined as the standard deviation of the ROI pixel intensities divided by the mean of the ROI pixel intensities.

D. Rat Skull Study

In this study, a 250-g rat was injected with 222 Mbq (6 mCi) ^{18}F-fluoride, a radiotracer preferentially taken up by bone. Imaging began 45 minutes post-injection. The rat was rotated 3 full revolutions over 3 hours while 1.5M counts were collected.

III. RESULTS

A. *Noise/Resolution Study*

We observed that the noise/resolution properties of 2D and 3D EM reconstructions after *n* iterations were nearly identical to those of OSEM with 5 subsets after *n*/5 iterations. The results in this section, presented as OSEM results, also hold for EM at the equivalent iteration, to within 3 or 4 digits of precision.

When comparing the resolution of different reconstructions, it is important that this be done at equivalent noise levels. This requires determining an appropriate stopping point for OSEM and a corresponding filter for the Fourier methods. Figure 2 plots noise in the central slice of the reconstructed cylinder background against radial resolution of the point source located at 8-mm radial offset in the central slice. Based on the noise/resolution tradeoff and computational considerations, we chose a stopping point for 3D OSEM of 10 iterations for these investigations; this is matched in noise to the 3DRP (Hann) result with 0.7 Nyquist cutoff frequency. Subsequent results were obtained using these parameters.

Transverse and coronal sections of the reconstruction of point sources in a warm cylinder are shown in Figure 3 for 3DRP Hann 0.7 and 3D OSEM-10 reconstructions. From the figure one can discern the resolution improvement achieved by 3D OSEM by the increased intensity of the point source. Figure 4 plots noise/resolution curves obtained by smoothing the result obtained from all four methods with a Gaussian filter. Notice that the unsmoothed 3D OSEM result ('B') possesses substantially improved resolution compared to the unsmoothed 3DRP Hann 0.7 result at matched noise ('A'). Alternatively, the smoothed 3D OSEM result ('C') achieves 40% lower noise at equivalent resolution compared to the unsmoothed 3DRP result.

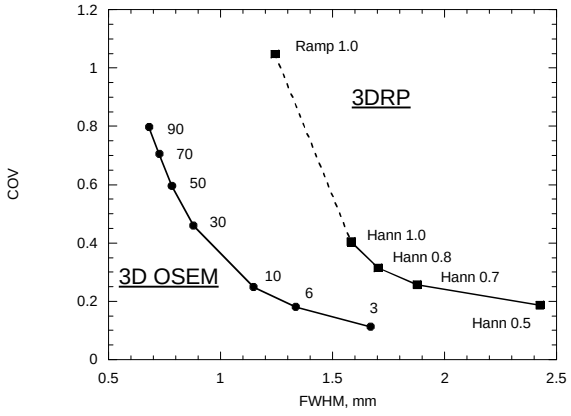

Figure 2: 3D Noise vs. radial resolution. The 3D OSEM plot is marked according to stopping iteration; the 3DRP plot is marked by filter and cutoff frequency relative to Nyquist.

In Figure 5A, axial noise profiles are plotted for the 4 methods (10 OSEM iterations and a Hann 0.7 filter). This result confirms that these parameters produce images with matched noise characteristics across the entire axial field of view of the algorithms over all slices for both 2D and 3D. In Figure 5B, the noise profiles for the 3D reconstructions were normalized to their respective average COV in the central slices. The 3D OSEM profile agrees with the predicted sensitiviy gain based on the relative axial acceptance angle for each slice. The deviations in the 3DRP profile from the predicted curve show the effect of smoothing in the edge slices which results from the use of reprojected LORs [14].

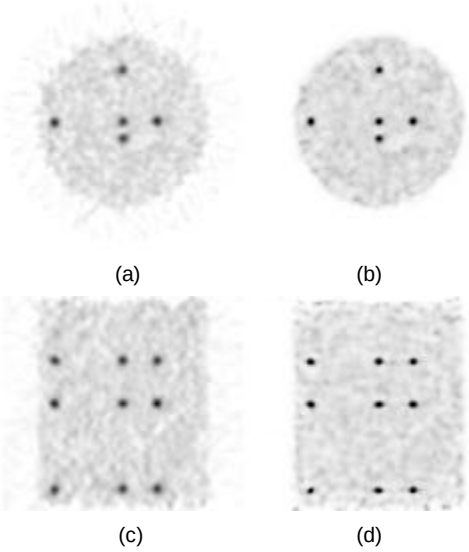

Figure 3: Reconstructed images of simulated point sources in a warm cylinder. (a) 3DRP central transverse section, (b) 3D OSEM central transverse section, (c) 3DRP central coronal section, (d) 3D OSEM central coronal section. Images are displayed on a common scale.

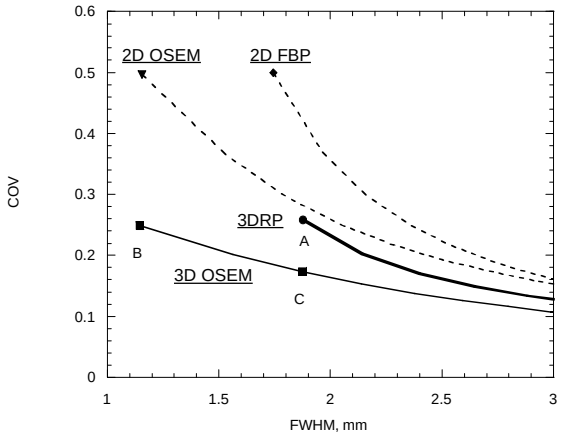

Figure 4: Noise vs. radial resolution for the 4 methods at various levels of smoothing.

In Figure 6A, radial, tangential, and axial resolution is plotted against radial position for the 3DRP Hann 0.7 and 3D OSEM-10 reconstructions. In Figure 6B, those same measures are plotted against axial position. The most striking observation in these plots is the significant improvement in OSEM resolution over 3DRP at all radial and axial locations. We have observed similar behavior in the resolution of the 2D reconstructions (results not shown). The resolution plots also indicate that in OSEM, axial resolution is somewhat better

than radial or tangential resolution. This could be due to the limited range of axial LOR angles accepted into the reconstruction. The depth of interaction effect, which is not corrected by the simple uniform resolution model used here, is thus less severe in the axial direction than in-plane.

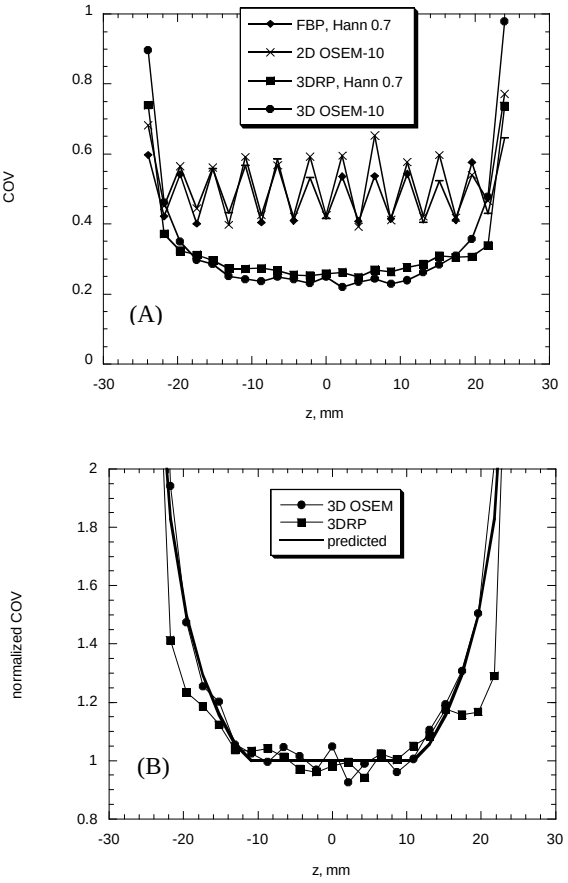

Figure 5: (A) - axial noise profiles for all methods. (B) - Noise profiles of 3D reconstructions, normalized against their average central-slice COV. Also plotted is the normalized predicted curve.

B. Rat Skull Study

A transverse section from the rat skull reconstructions is shown in Figure 7 for the 4 methods. Figure 8 displays coronal and sagittal sections for each of the 3D reconstructions. The images are displayed on a common scale, normalized to total activity. The most prominent feature in these images is the mandible. Visual assessment of these images suggests that the resolution of the OSEM result is higher. For example, certain small bones are resolvable only in the 3D OSEM result. Noise measured in a background ROI indicates roughly equivalent COVs between 3DRP and 3D OSEM. This observation is consistent with our finding of improved resolution at matched noise levels.

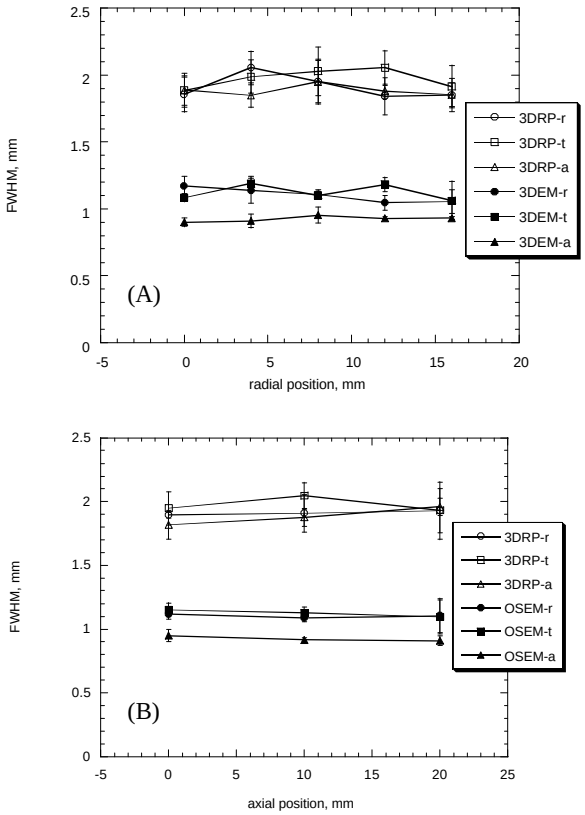

Figure 6: Radial (r), tangential (t), and axial (a) resolution of 3D reconstructions against radial position (A) and axial position (B).

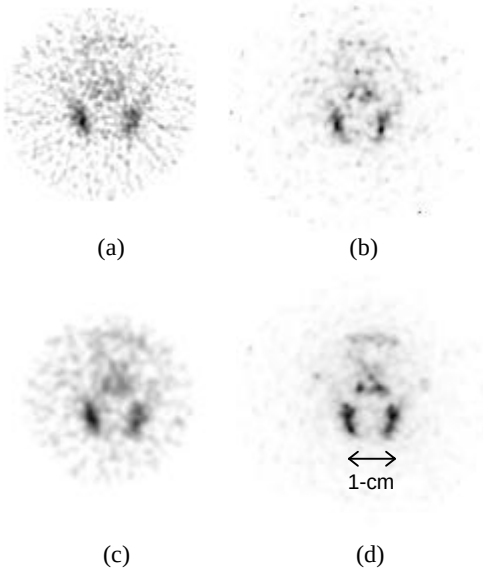

Figure 7: Transverse section of the reconstructed rat skull. (a) FBP Hann 0.7, (b) 2D OSEM-10 , (c) 3DRP Hann 0.7, (d) 3D OSEM-10. Images are displayed on a common scale, normalized to total activity.

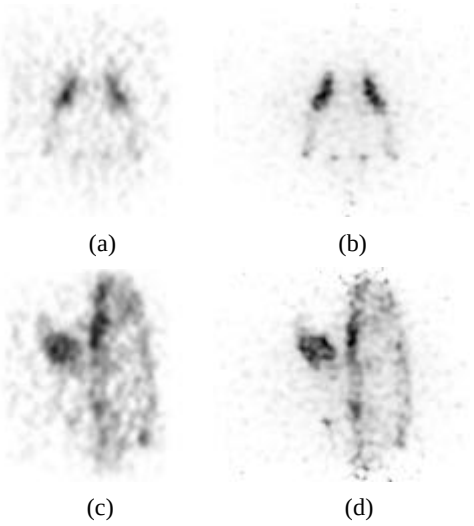

Figure 8: Coronal and sagittal sections of the rat skull reconstruction. (a) 3DRP Hann 0.7 coronal, (b) 3D OSEM Hann 0.7 coronal, (c) 3DRP-10 sagittal, (d) 3D OSEM-10 sagittal.

IV. DISCUSSION

For count-limited studies, the ability of EM and OSEM to neglect projection lines with zero counts (98% in the rat skull study) improves the computational requirement considerably and makes EM algorithms feasible for routine reconstructions of data from this scanner. In Table 1 we compare computational requirements of the various algorithms for the rat skull reconstruction including conventional EM and OSEM using 23 thick (2.1-mm) slices as well as 107 thin (0.47-mm) slices. Observe that the cost of performing a thin-slice 3D reconstruction in OSEM is only 2.3 times the computational cost of reconstructing thick slices. Had all coincidence lines been 'occupied', the factor would have been greater than 16. Using 16 IBM SP2 nodes, the total time required to reconstruct a 1.5M count rat skull with thin slices is 76 minutes. OSEM iterations require slightly more time than EM iterations. This discrepancy can be reduced by better load balancing in OSEM, where the parallel partitioning is constrained within a subset.

Table 1: Computational requirements of the various algorithms to reconstruct the [F-18] rat skull images. Reconstructions were performed on 66-MHz IBM SP2 CPUs.

method	# slices	CPUs	iteration time, min.	iters. used	total time, min.
3D EM	23	16	2.76	50	138
3D EM	107	16	6.8	50	340
2D OSEM	23	4	1.1	10	11
3D OSEM	23	16	3.28	10	33
3D OSEM	107	16	7.58	10	76

We have observed that EM reconstructions taken to n iterations have nearly identical noise/resolution properties as OSEM reconstructions taken to $n/5$ iterations when 5 OSEM subsets were used. The OSEM algorithm, however, does not converge to the maximum likelihood solution [15]. The reconstructions being reported here are far from convergent. We can only infer from our findings that, at early iterations, EM and OSEM produce nearly equivalent iterates as defined by certain image quality measures.

In this paper we consider the noise/resolution properties of a class of low-count, finely sampled (in projection space) reconstructions. The improvement in resolution between EM/OSEM and Fourier-based methods on these data is greater than we have observed with clinical PET data. The small animal scanning situation differs from clinical machines in that sampling is much finer and the number of counts per bin is very low. Thus, EM and OSEM reconstructions at relatively low iterations appear to provide a resolution advantage at matched noise levels over Fourier-based reconstructions for the scanner being considered here.

A caveat is in order. EM and OSEM can incorporate a spatially variant scanner resolution model into the algorithm and, in effect, perform resolution recovery during the reconstruction process. No resolution recovery was attempted on the Fourier-based results. A well-designed Wiener filter applied to the Fourier-based reconstructions may produce better results for FBP and 3DRP than we are reporting.

Opposed-mode NaI(Tl) cameras with thin detectors have high resolution but poor sensitivity. Although the results obtained from OSEM reconstructions in this paper are encouraging, the poor sensitivity of NaI(Tl) limits its applicability. A small field-of-view LSO camera can offer a substantial improvement in sensitivity at nearly the resolution of the NaI(Tl) camera [16]. An LSO system allows for the possibility of biologically relevant scan durations and dynamic studies with statistical noise comparable to that seen in the NaI(Tl) system. We therefore believe that the apparent benefits of EM and OSEM seen here will again be realized for the LSO system.

V. REFERENCES

[1] P.M. Bloomfield, S. Rajeswaran, T.J. Spinks, S.P. Hume, R. Myers, S. Ashworth, K.M. Clifford, W.F. Jones, L.G. Byars, J. Young., M. Andreaco, C.W. Williams, A.A. Lammertsma, and T. Jones, "The design and physical characteristics of a small animal positron emission tomograph," *Phys. Med. Biol.*, vol. 40, pp. 1105-1126, 1995.

[2] S. Rajeswaran, D.L. Bailey, S.P. Hume, D.W. Townsend, A. Geissbuhler, J. Young, and T. Jones, "2-D and 3-D imaging of small animals and the human radial artery with a high resolution detector for PET," *IEEE Trans. Med. Imag.*, vol. 11, pp. 386-391, 1992.

[3] R.S. Miyaoka, A.N. Bice, M. Muzi, and T.K. Lewellen, "Dynamic high resolution imaging for rats: quantitative potentials," in Conference Record, in *IEEE Nucl. Science Symp. and Medical Imaging Conf.*," pp. 1673-1677, 1991.

[4] R.E. Carson, Y. Yan, B.Chodkowski, T.K. Yap, and M.E. Daube-Witherspoon, "Precision and accuracy of regional radioactive quantitation using the maximum likelihood EM reconstruction algorithm," *IEEE Trans. Med. Imag.*, vol 13., pp. 526-537, 1994.

[5] J.S. Liow and S.C. Strother, "Noise and signal decoupling in maximum likelihood reconstructions and Metz filters for PET images," *in IEEE Nucl. Science Symp. and Medical Imaging Conf.*, pp. 901-903, 1992.

[6] A.A. Lammertsma, S.P. Hume, R. Myers, S. Ashworth, P.M. Bloomfield, S. Rajeswaran, T. Spinks, and T. Jones, "PET scanners for small animals," *J. Nucl. Med.*, vol. 36, pp. 2391-2392, 1995.

[7] J. Seidel, W.R. Gandler, and M.V. Green, "A very high resolution single-slice animal PET scanner based on direct detection of coincidence line endpoints," *J. Nucl. Med.*, vol. 35, p. 40P, 1994.

[8] P.E. Kinahan and J.S. Karp, "Figures of merit for comparing reconstruction algorithms with a volume-imaging PET scanner," *Phys. Med. Biol.*, vol. 39, pp. 631-642, 1994.

[9] P.E. Kinahan and J.G. Rogers, "Analytic 3D image reconstruction using all detected event," *IEEE Trans. Nucl. Sci.*, vol. 36, pp. 964-968, 1988.

[10] J.S. Liow, S.C. Strother, and D.A. Rottenberg, "Improved resolution via 3D iterative reconstruction for PET volume imaging," in *IEEE Nucl. Science Symp. and Medical Imaging Conf.*, pp. 1315-1319, 1994.

[11] J. Liow and S. Strother, "Practical tradeoffs between noise, quantitation and number of iterations for maximum likelihood-based reconstructions," *IEEE Trans. Med. Imag.*, vol. 10, pp. 563-571, 1991.

[12] H.M. Hudson and R.S. Larkin, "Accelerated image reconstruction using ordered subsets of projection data," *IEEE Trans. Med. Imag.*, vol. 13, pp. 601-609, 1994.

[13] C.A. Johnson, Y. Yan. R.E. Carson, R.L. Martino, and M.E. Daube-Witherspoon, "A system for the 3D reconstruction of retracted-septa PET data using the EM algorithm," *IEEE Trans. Nucl. Sci.*, vol. 42, pp. 1223-1227, 1994.

[14] S. Pajevic, M.E. Daube-Witherspoon, S.L. Bacharach, and R.E. Carson, "Noise characteristics of 3D and 2D PET images," submitted to *IEEE Trans. Med. Imag.*

[15] J. Browne and A.R. DePierro, "A row-action alternative to the EM algorithm for maximizing likelihoods in emission tomography," *IEEE Trans. Med. Imag.*, vol. 15, no. 5, pp. 687-699, 1996.

[16] J. Seidel, W.R. Gandler, and M.V. Green, "Characteristics of a pair of small field-of-view LSO scintillation cameras," *IEEE Trans. Nucl. Sci.*, vol. 43, pp. 1968-1973, 1996.

* Ariela Sofer is partially supported by NSF grant DMI-9414355.